

Small-angle neutron scattering study of micropore collapse in amorphous solid water†

Cite this: *Phys. Chem. Chem. Phys.*,
2014, **16**, 16013

Christian Mitterdorfer,^a Marion Bauer,^b Tristan G. A. Youngs,^c Daniel T. Bowron,^c
Catherine R. Hill,^d Helen J. Fraser,^d John L. Finney^e and Thomas Loerting^{*a}

Vapor-deposited amorphous solid water (ASW) is the most abundant solid molecular material in space, where it plays a direct role in both the formation of more complex chemical species and the aggregation of icy materials in the earliest stages of planet formation. Nevertheless, some of its low temperature physics such as the collapse of the micropore network upon heating are still far from being understood. Here we characterize the nature of the micropores and their collapse using neutron scattering of gram-quantities of D₂O–ASW of internal surface areas up to $230 \pm 10 \text{ m}^2 \text{ g}^{-1}$ prepared at 77 K. The model-free interpretation of the small-angle scattering data suggests micropores, which remain stable up to 120–140 K and then experience a sudden collapse. The exact onset temperature to pore collapse depends on the type of flow conditions employed in the preparation of ASW and, thus, the specific surface area of the initial deposit, whereas the onset of crystallization to cubic ice is unaffected by the flow conditions. Analysis of the small-angle neutron scattering signal using the Guinier–Porod model suggests that a sudden transition from three-dimensional cylindrical pores with 15 Å radius of gyration to two-dimensional lamellae is the mechanism underlying the pore collapse. The rather high temperature of about 120–140 K of micropore collapse and the 3D-to-2D type of the transition unraveled in this study have implications for our understanding of the processing and evolution of ices in various astrophysical environments.

Received 10th February 2014,
Accepted 17th June 2014

DOI: 10.1039/c4cp00593g

www.rsc.org/pccp

Amorphous solid water (ASW) is the dominant phase of ice in the universe, even though it does not naturally form on Earth. The most widespread occurrence of ASW is on interstellar dust, in comets and many solar-system bodies.^{1–4} It may occasionally form in the coldest region of Earth's atmosphere, near the mesopause at altitudes of about 80 km, when temperatures drop below 150 K.⁵ Amorphous solid water (ASW) accretes onto dust particles in the cold regions of dense interstellar clouds, where it plays a key role in promoting chemical reactions, acting as a reservoir trapping volatile gases, and potentially is pivotal in the earliest stages of planet building.⁶ On interstellar dust particles ASW may form by chemical vapour deposition at

10 K, involving reaction of O, H, O₂, H₂ and OH, or by direct water vapour deposition onto dust particles. While the former is the dominant mechanism in cold dark star-forming clouds,^{7,8} the latter dominates in shocked regions and discs.⁶ In the laboratory it is typically produced by deposition of water vapor onto cold substrates; a process that was reported for the first time in 1935 by Burton and Oliver.⁹ In terms of radial distribution functions,^{10–13} ASW is similar to hyperquenched glassy water,¹⁴ which is prepared by ultrafast cooling of liquid water droplets,¹⁵ and low-density amorphous ice, which is prepared by pressure-induced amorphization of ice at 77 K and >1.2 GPa (resulting in high-density amorphous ice),¹⁶ followed by bringing the sample to ~140 K at 0–0.1 GPa.^{17,18} The morphology of the ASW formed depends on the deposition conditions, especially the flow rate and directionality, substrate temperature, and water partial pressure.^{19–21} When the deposition temperature is increased from <10 K to >200 K the ice phase deposited changes from porous ASW² and compact ASW to cubic and hexagonal ice. This transition sequence is also observed when heating ASW deposited at low temperature. The bulk density (disregarding pores) of these ice forms is $0.93 \pm 0.01 \text{ g cm}^{-3}$. At very low deposition temperatures an ASW form of higher bulk density may form.^{22,23}

The collapse of the pore network marking the transition from porous to compact ASW is still not understood, in spite of

^a Institute of Physical Chemistry, University of Innsbruck, Innrain 52a,
A-6020 Innsbruck, Austria. E-mail: thomas.loerting@uibk.ac.at

^b Institute of General, Inorganic and Theoretical Chemistry, University of Innsbruck,
Innrain 52a, A-6020 Innsbruck, Austria

^c ISIS Facility, Rutherford Appleton Laboratory, Harwell Oxford, Didcot,
Oxon OX11 0QX, UK

^d Department of Physical Sciences, The Open University, Walton Hall,
Milton Keynes MK7 6AA, UK

^e Department of Physics and Astronomy and London Centre for Nanotechnology,
University College London, Gower Street, London WC1E 6BT, UK

† Electronic supplementary information (ESI) available. See DOI: 10.1039/c4cp00593g

a large number of experimental and theoretical studies related to dangling OH-bonds,^{21,24–30} gas-adsorption^{30–35} and desorption^{36–43} or positron spectroscopy.^{44–46} A comparison of results obtained in different laboratories is not straightforward because widely different deposition techniques and flow conditions are employed, which result in ASW samples of different morphology (thin-film vs. granular bulk samples), surface area and contamination levels. However, a massive reduction of surface area from up to several hundred $\text{m}^2 \text{g}^{-1}$ in porous ASW to less than one $\text{m}^2 \text{g}^{-1}$ in compact ASW is unquestionable. The pore diameters were found to be less than 21 Å, which places them in the category of micropores.^{2,44} The decline in microporosity at 90–130 K^{33,36,45} was recently suggested to be preceded by pore clustering at <90 K.⁴⁵ However, the nature of the pore-collapse itself, the connectivity of the pores and the shape of the pores have remained elusive. Most often a spherical nature of the pores is assumed. This is, however, not the case according to our analysis of the structure and pore-collapse in ASW presented below.

Small angle neutron or X-ray scattering are non-destructive methods particularly suited to study granular or porous structures with dimensions between 10 and 1000 Å.⁴⁷ The techniques have been applied successfully, *e.g.*, by Buiel *et al.* to study the transformation from open to closed pores of hard carbon samples between 900 and 1400 °C,⁴⁸ by Walter *et al.* to study growth of pore-channels in porous glasses,⁴⁹ and by Antropova *et al.* to follow macropore collapse in alkali-borosilicate glasses.⁵⁰ In spite of the powerful potential of small-angle scattering for studying pores at the micro- and macroscale, this technique has not been applied to the study of the pore-collapse in ASW, probably due to the difficulty in producing gram-quantities of D₂O-ASW (rather than thin-films) and the need to transfer these samples to the neutron source. NIMROD – the Near- and InterMediate Range Order Diffractometer – of the ISIS Second Target Station (a neutron spallation source) has the ability to measure on a continuous length scale from <1 to >300 Å.⁵¹ Its recent inauguration provided us with the unique capability of measuring the small-angle neutron scattering signal ($Q < 1 \text{ \AA}^{-1}$) simultaneously with the large-angle neutron scattering signal ($Q > 1 \text{ \AA}^{-1}$). While the former carries information on the pore-structure of the ASW samples, the latter carries information about the short-, intermediate- and long-range ordering of the water molecules. The latter has been used by some of us in combination with isotope substitution to study a range of amorphous ices, including annealed/compact ASW, and to generate structural models based on the radial distribution functions.^{13,52–54} In the present study the process of pore-collapse can be monitored in the small-angle signal, whereas crystallization of the amorphous ice network is immediately evident in the large-angle signal.

The vapor deposits were produced with the apparatus depicted in Fig. 2 of ref. 55 using the technique described therein. In brief, D₂O vapor is deposited on a cold plate made from copper, which is in direct contact with liquid nitrogen. Background pressure is 1×10^{-4} mbar and during deposition the water pressure is increased to 0.1 mbar (“slow” deposition) or 0.3 mbar (“fast” deposition) by opening a needle valve

connected to a D₂O reservoir (Deuterium oxide 99,8 Atom%D – Carl ROTH). Deposition times were between 24 and 30 hours at growth rates of about 40 μm per hour for the former and 130 μm per hour for the latter. The deposition is either done as a line of sight deposition (“non-baffled, supersonic flow”) or by back-ground deposition (“baffled flow”)⁵⁵ and allow producing the gram-quantities required in neutron diffraction experiments. During the deposition procedure the temperature is 77 K at all times. In comparison to many thin film experiments the deposition rates and temperatures are higher. While one might predict highly compact ASW (cASW, which still shows porosity) would be formed under such conditions,⁵⁶ in fact a highly porous ASW (pASW) forms. In total four D₂O-ASW 77 K deposits were generated for neutron diffraction experiments – namely baffled and non-baffled samples with high and low deposition rate. Similarly prepared samples were previously characterized by calorimetry,^{55,57} dielectric relaxation,⁵⁸ BET isotherms using nitrogen as adsorption gas,³¹ IR spectroscopy,^{59,60} and diffraction^{12,13} by the Innsbruck group. The BET surface area of all samples before pore collapse is about 220–240 $\text{m}^2 \text{g}^{-1}$. After deposition the ASW was scraped off the copper plate under liquid nitrogen with a spatula, stored as granular material in liquid nitrogen and shipped to ISIS. The granules were then transferred under liquid nitrogen into a null-scattering TiZr alloy cell, compacted with a spatula and placed immediately into a Helium cryostat. Thus, the sample temperature was kept at 77 K at all times. Scattered intensities were recorded in the following way: first the samples were held at 90 K for 30 minutes, recording the neutron scattering continually, then the temperature was increased by 10 K (heating rate of 0.3 K min^{-1}) and data collected for another 30 minutes, where a further neutron scattering measurement was made. The sample temperature was increased to at least 160 K, where full crystallization to cubic ice was observed. This temperature program was applied to all four samples.

The scattered intensities of all four investigated specimens at 90–160 K are depicted in Fig. 1 in the Q range from 0.01 to 50 \AA^{-1} , a range which can be covered in a single NIMROD measurement. For the further discussion it is useful to divide the Q -range into two parts, namely below and above 1 \AA^{-1} . First, let us consider the small angle neutron scattering (SANS) signal. Owing to the heterogeneous nature of the ASW matrix there is high intensity in the low Q -range. The main feature seen in the SANS signal is a shoulder (“hump”, “knee”) at approximately 0.1 \AA^{-1} . This feature is there for all scattering curves recorded at $T < 120$ K, but not at higher temperatures, and indicates the microporous nature at $T < 120$ K, which disappears at higher temperatures. In the case of baffled samples, the knee disappears first at 120 K, whereas for the non-baffled samples this occurs at a temperature of 140 K, always independently of deposition rates. Interestingly, this knee in the scattered intensities does not shift significantly to higher or lower Q -values, which would indicate pore size shrinkage or growth. Merely a flattening of the scattered intensity between 0.01 and 1 \AA^{-1} is observed, which implies a shape change and testifies that pore-collapse is more complex

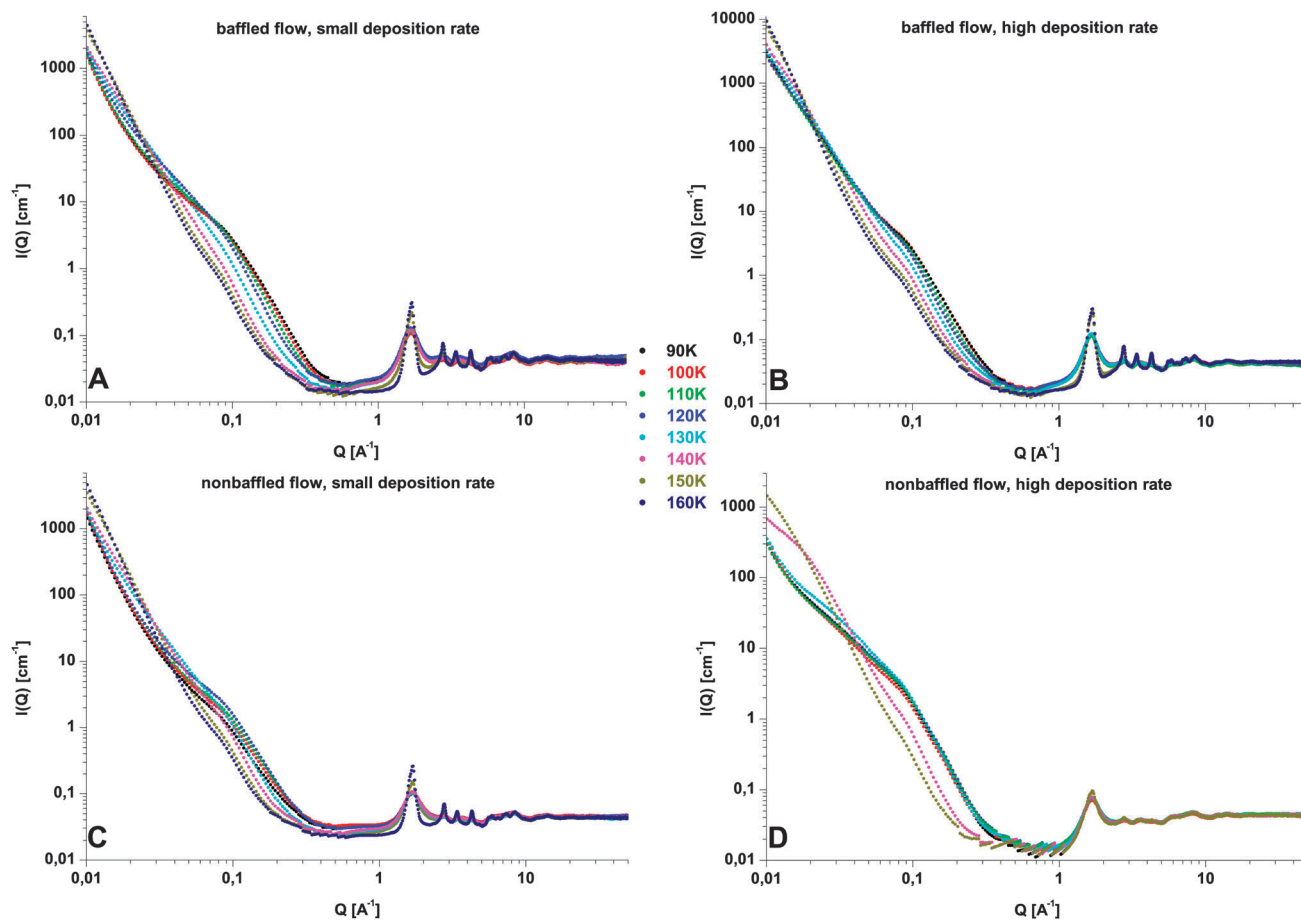


Fig. 1 Temperature evolution between 90 and 160 K of the scattered intensity for the whole available Q -range (0.01 – 50 \AA^{-1}) for different deposition conditions. (A) Baffled flow, small deposition rate, (B) baffled flow, high deposition rate, (C) non-baffled flow, small deposition rate and (D) non-baffled flow, high deposition rate. Error bars on the data points are about the symbol size.

than previously thought. Furthermore the scattered intensity still shows a strong signal after crystallization to cubic ice. This implies that the small angle scattering signal has besides micropores other contributions. We attribute this to the granular nature of the material. Individual grains are up to a few mm long and up to approximately 0.5 mm in diameter. While scattering from these very large grains themselves does not contribute significantly, scattering from the grain surfaces and junctions contributes to the small angle scattering signal. Boxe *et al.* utilized electron scanning microscopy and observed in the temperature range 90 to 123 K small amorphous particles between 0.2 and 0.4 \mu m in amorphous solid water films,³⁴ which increase to $\sim 1 \text{ \mu m}$ after crystallization.³⁴ For the reason of the different sizes involved in the scattering process the power law scattering below 0.1 \AA^{-1} arises mainly from the grain surfaces and interfaces, whereas the power law scattering above 0.1 \AA^{-1} arises mainly from the microporosity.⁶¹

The scattered intensity in the intermediate Q -range can be utilized to infer crystallization of the amorphous material to cubic ice. For temperatures $T > 150 \text{ K}$ sharp Bragg peaks develop between 1 and 10 \AA^{-1} , e.g., the $[1\ 1\ 1]$, $[2\ 2\ 0]$, $[2\ 2\ 2]$ and $[3\ 3\ 1]$ cubic ice reflections, which become even sharper at higher temperature. This clear evidence for the crystallization

to cubic ice is only evident at $T > 150 \text{ K}$, but not below. We can therefore conclude that the flattening of the SANS signal at 120 K for baffled and 140 K for non-baffled samples is not related to crystallization, but rather to the morphological change of pore-collapse in ASW. The Porod exponent d (see eqn (2)) is found to be 4 in the Q -range 0.1 – 0.3 \AA^{-1} . At $Q < 0.03 \text{ \AA}^{-1}$ the Porod exponent d increases with increasing temperature from 3 to almost 4 . This reflects scattering from the grain surfaces and changes in the surface roughness with temperature, especially upon crystallization.

The raw data are analysed with different approaches: the first one is a model independent analysis. In addition we have tried to fit our data to models of small angle scattering. First, we have attempted to use a model assuming a spherical pore shape and a Maxwellian pore size distribution. As described and shown in the ESI† this model does not capture the physics of ASW pore-collapse as known from literature. By contrast, the second model (“new Guinier–Porod model”) is able to capture the pore-collapse from the data by allowing for non-spherical pores.⁶² This model contains a sphericity factor, s , as an indicator of pore shape. After explaining briefly the two concepts, the main results of the data analysis are presented.

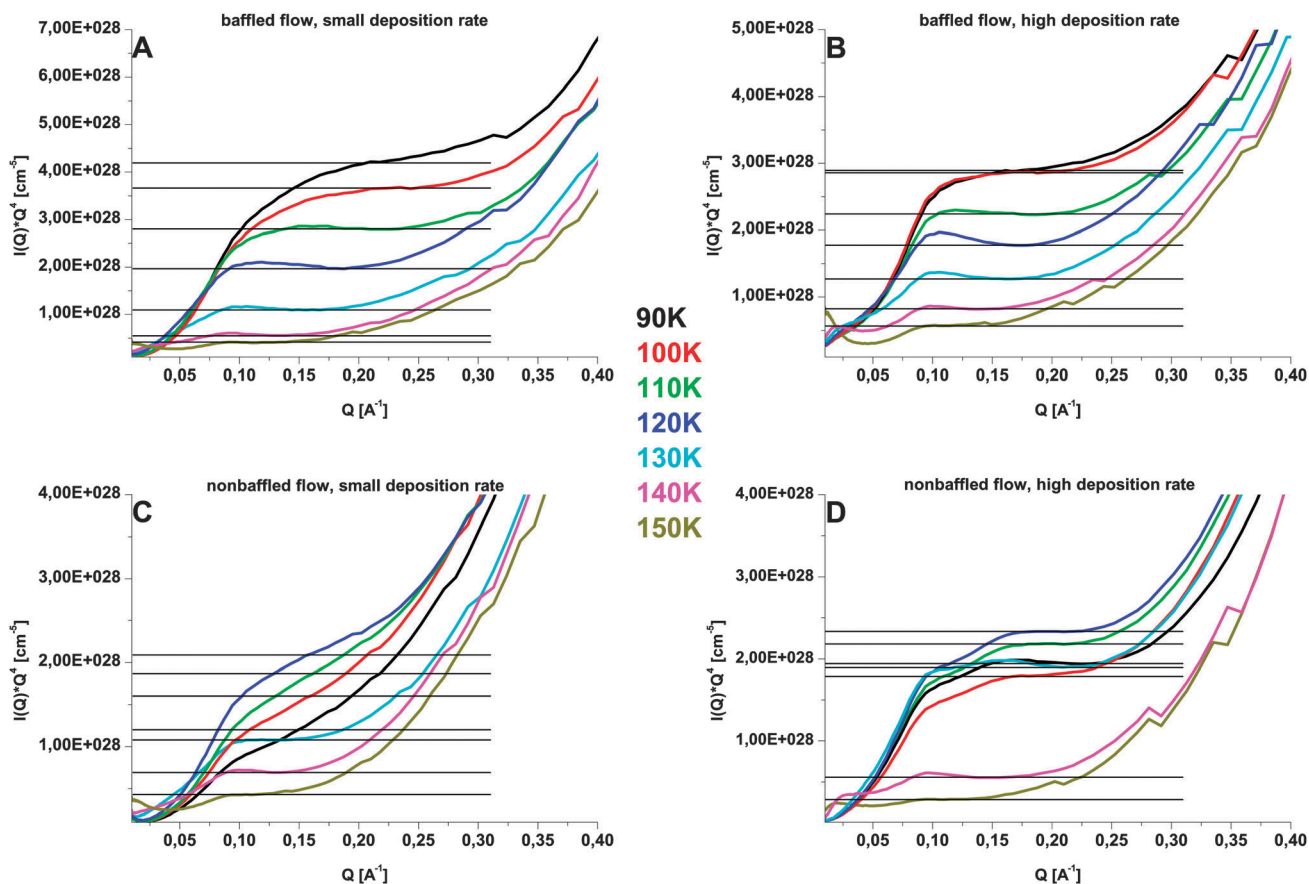


Fig. 2 Temperature evolution between 90 and 150 K of Porod plots $I(Q) \cdot Q^4$ versus Q for different deposition conditions. (A) Baffled flow, small deposition rate, (B) baffled flow, high deposition rate, (C) non-baffled flow, small deposition rate and (D) non-baffled flow, high deposition rate.

The scattered intensity at small angles provides an absolute scale (in cm^{-1}), from which the specific surface area can be extracted. According to Paglia *et al.* the specific surface area Σ_S is obtained from eqn (1), where ρ_m is the mass density of the solid, $\Delta\rho^2$ the scattering contrast and K the Porod constant.⁶³ $\Delta\rho$ is the difference between the scattering length densities of deuterated water and empty pores and thus can be calculated. The Porod constant for the four samples studied is determined as a function of sample temperature from the intercepts of the (quasi)-plateaus in the $I(Q) \cdot Q^4$ plots (horizontal lines in Fig. 2)

$$\Sigma_S = \frac{1}{\rho_m} \cdot \frac{\lim_{Q \rightarrow \infty} (I(Q) \cdot Q^4)}{2\pi\Delta\rho^2} = \frac{1}{\rho_m} \cdot \frac{K}{2\pi\Delta\rho^2} \quad (1)$$

We note that not all plots show real plateaus, but instead sloped linear regimes. In these cases we have taken the “half-way” point and extracted error bars from the onset and endpoints of the (sloped) plateaus. The specific surface areas deduced in this manner from the model-independent analysis are summarized in Fig. 3. Whereas the specific surface areas extracted from the small angle data agree very well with the results obtained from the BET analysis of nitrogen adsorption in case of the baffled-flow conditions, the specific surface areas

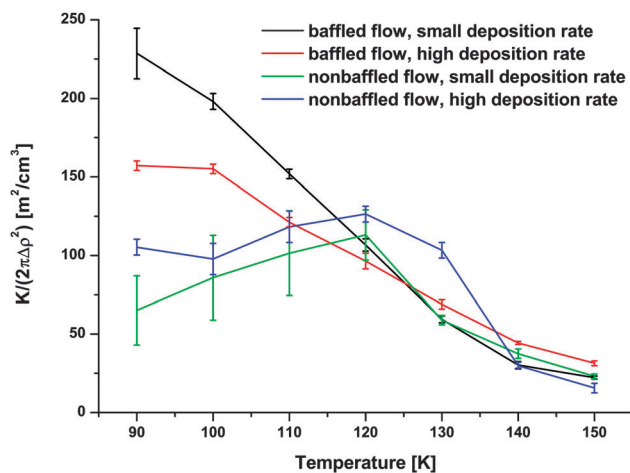


Fig. 3 Temperature evolution between 90 and 150 K of the specific surface area (SSA) in $\text{m}^2 \text{cm}^{-3}$ for different deposition conditions obtained from the Porod plots (Fig. 2). Error bars were estimated from the slopes of the (quasi)-plateaus in Fig. 2.

of the non-baffled samples are lower by about a factor of 2 than the BET result of $230 \text{ m}^2 \text{g}^{-1}$. Upon heating, the baffled-flow samples exhibit a continuous decrease of the specific surface area between 90 and 150 K, whereas the non-baffled flow

specimens feature a slight increase in the specific surface area between 90 and 120 K, and start to decrease suddenly at ≥ 120 K. This behaviour is also evident when comparing the intensities in the Porod plots $I(Q) \cdot Q^d$ for the baffled *versus* nonbaffled flow samples at different temperatures. This increase may be attributed to pore-clustering, which takes place prior to the pore-collapse, as also suggested in recent work.⁴⁵

In addition to the Porod plots for each sample further standard linear plots $I(Q) \cdot Q^d$ (with d equal 2.5 or 3.0) *versus* Q are depicted in Fig. 4. These plots transform the “knee” at approximately 0.1 \AA^{-1} into a more pronounced peak – sometimes referred to as “pseudopeak”. Hass *et al.* mentions that interference peaks in these plots hint at periodic spacings.⁶⁴ The Q -values of the peaks in Fig. 4 correspond to d -spacings of approximately 60 and 77 \AA ($d = 2\pi/Q$), which represents the “pseudo”-periodicity, *i.e.*, the average distance between the micropores. The pronounced peaks are present up to 120 K for all specimens and disappear at 130 K for baffled-flow and at 140 K for non-baffled flow samples, which again indicates that the pore-collapse occurs rather suddenly above these temperatures. That is, the pseudo-periodicity of micropores is more stable for non-baffled samples. Furthermore the position of the peak is stable at approximately 70 \AA for the nonbaffled flow

samples, but exhibits a slight drift for the baffled samples. Thus, the model-free interpretation of the small-angle data suggest that there is a competition between pore-clustering and micropore collapse, where the micropore-collapse starts to be dominant above 130 K for baffled-samples and above 140 K for the non-baffled samples.

In order to shed more light on the nature of the micropore-collapse itself we have applied various models to the small-angle data. None of the models assuming spherical pores is able to capture the features in the data. We exemplify this in the ESI† on the example of assuming a Maxwell distribution of spherical pores. This model does not reveal any change of the pore size in the whole temperature region, and is thus unphysical. Instead of spherical models, we, therefore, use in addition to the model-free approach a second approach to model also the pore-sizes and pore-shapes. The “new Guinier–Porod model” was developed by Hammouda⁶² and provides a data analysis route that is an alternative to the standard linear plots (Guinier, Porod, Kratky, *etc.*).⁶² Hammouda defines a dimensionality parameter $3-s$, where $s = 1$ correlates with a cylindrical pore geometry, $s = 2$ is equivalent to a platelet structure and $s = 0$ corresponds to a spherical pore.⁶² The modified expressions for the Guinier and Porod term are the

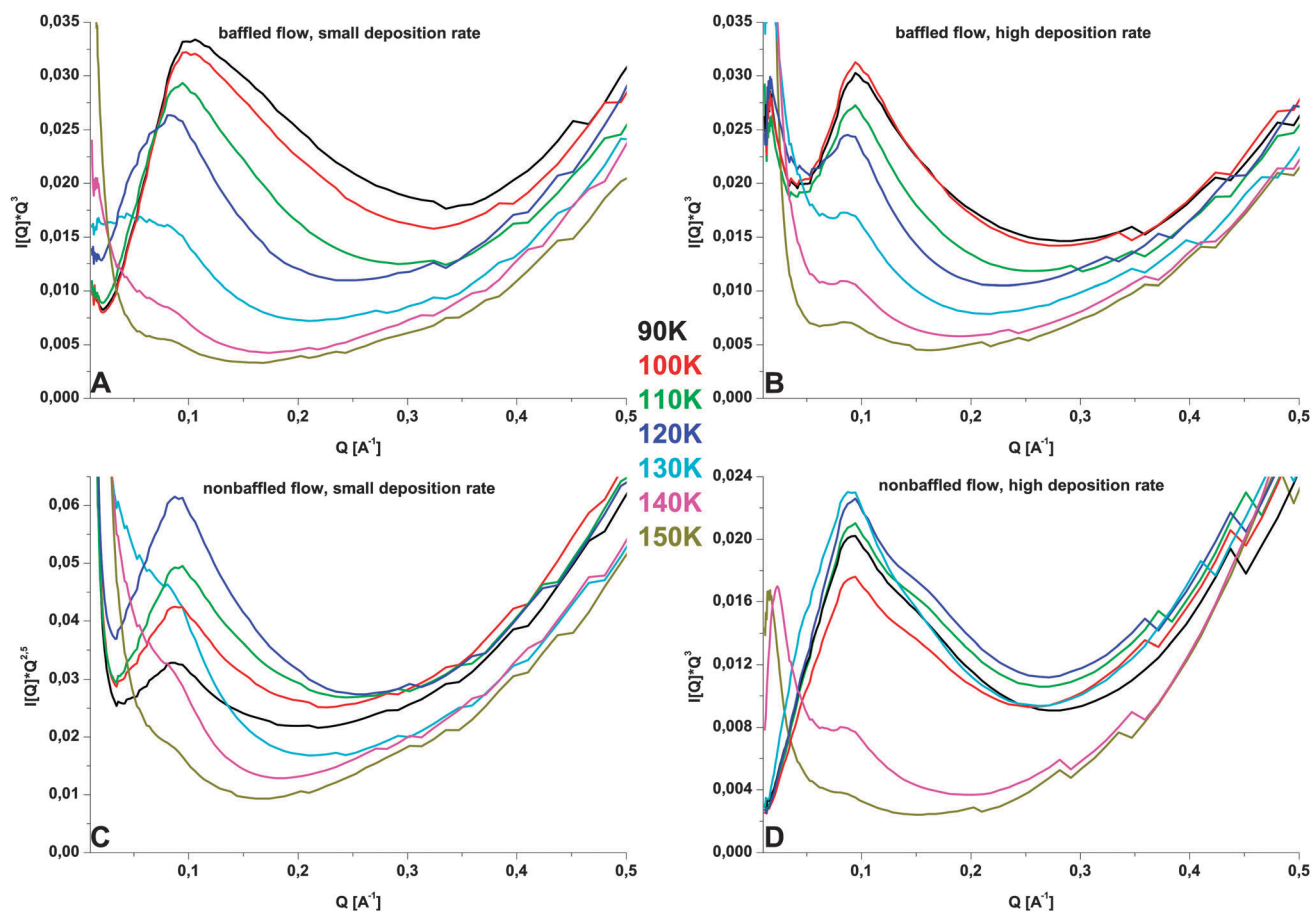


Fig. 4 Temperature evolution between 90 and 150 K of standard linear plots $I(Q) \cdot Q^d$ *versus* Q with d between 2, 5 and 3. (A) Baffled flow, small deposition rate with $d = 3$, (B) baffled flow, high deposition rate with $d = 3$, (C) non-baffled flow, small deposition rate with $d = 2.5$ and (D) non-baffled flow, high deposition rate with $d = 3$.

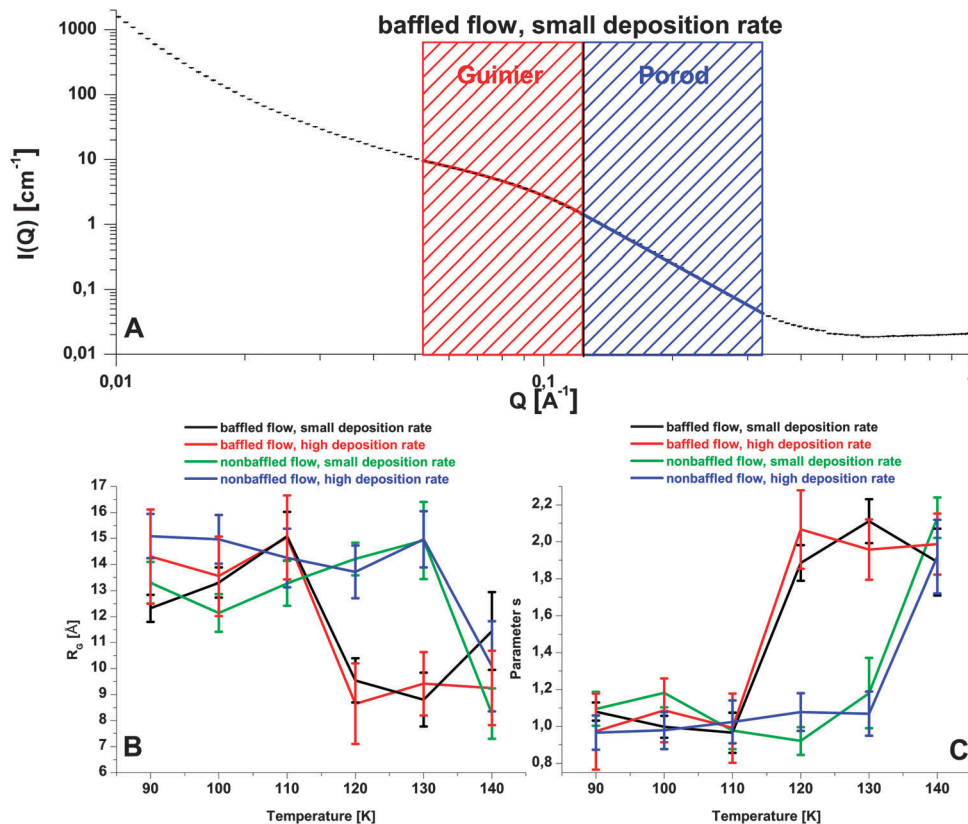


Fig. 5 Data evaluation by a new Guinier–Porod model in the low Q -range. (A) Scattered intensity in the low Q -region ($0.01\text{--}1\text{ \AA}^{-1}$) including the Guinier and Porod region. Error bars on the data points themselves are indicated. (B) Temperature development of the radius of gyration between 90 and 140 K for all four specimens. (C) Temperature evolution of the Parameter s between 90 and 140 K for all four specimens.

following,⁶² where R_G is the radius of gyration and G and D are the Guinier- and Porod-scaling factors, respectively.

$$I(Q) = \frac{G}{Q^s} \cdot \text{Exp}\left(-\frac{Q^2 \cdot R_G^2}{3-s}\right) \quad Q \leq Q_1 \quad (2)$$

$$I(Q) = \frac{D}{Q^d} \quad Q \geq Q_1$$

Part A of Fig. 5 illustrates the two fitting regions, namely the Guinier region for $Q \leq Q_1$ and the Porod region for $Q \geq Q_1$, where the Guinier region is dominated by contributions from the micropores. The scattered intensities for the four specimens and all temperatures up to 140 K were fitted with eqn (2). The results for the Guinier region are summarized in Fig. 5B and C, which present the radius of gyration plus the parameter s as a function of the temperature. The variance in the fit parameters determines the size of the error bars. Baffled flow samples feature a simultaneous, very sudden change in the radius of gyration and the parameter s at $T = 120$ K, in agreement with the model-free approach. For the non-baffled flow specimens the same happens at $T = 140$ K, indicating a higher stability against pore collapse of these samples, and again in agreement with the model-free approach.

Based on this “new Guinier–Porod model” the pores undergo, therefore, a transition from a cylindrical geometry ($s = 1$) to a

platelet-like structure ($s = 2$), *i.e.*, a transition from three-dimensional structure to a two-dimensional structure. That is, our analysis suggests the pores to be of cylindrical shape at 90–110 K with a radius of gyration of about 15 Å, which remain unchanged on the time-scale of about an hour. In case of non-baffled flow, the cylindrical pores remain unaffected even at 130 K on this time-scale. However at 120 K or 140 K (baffled and non-baffled flow samples, respectively), a relatively sudden change takes place, and the pores appear to be “squashed” to lamellae, *i.e.*, they experience a 3D to 2D transition. A detailed analysis of the kinetics of the collapse process will be reported elsewhere.

This phenomenology is quite similar to the finding of a cylindrical to lamellar transition for the poloxamer Pluronic P85 in deuterated water.⁶⁵ We here infer a rather sudden 3D to 2D transition that is preceded by gradual specific surface-area reduction and/or pore-clustering. In other work the gradual nature^{21,45,46,56} over a broad temperature range has also been found, but not the sudden transition. It may be the case that the sudden collapse of the pores can not be inferred easily, *e.g.*, by observing the dangling OH modes. This finding together with our observation of the different collapse temperature in baffled and non-baffled ASW samples implies that the stability of the pore-structure in ASW critically depends on the growth conditions of ASW. We assume that baffled flow is mainly characterized by deposition of water monomers on the surface

(which produces rather flat ASW samples), whereas in case of non-baffled flow line of sight deposition of water–oligomers may play a more important role (which produces tower-like ASW structures resembling stalactites). Why the latter results in more stable pore networks than the former needs to be answered by additional experimental studies allied to appropriate simulation work. In contrast, the different deposition rates used here (40 vs. 130 μm per hour) do not seem to change significantly the stability of the pore network against collapse. Whereas the deposition mode affects the stability against pore collapse and the pore-clustering process preceding the collapse, the crystallization to cubic ice is not affected at all – all samples crystallize at the same temperature.

This sudden transition from a 3D to 2D situation may have interesting astrophysical implications. For instance the rate of formation of H_2 molecules from H atoms may be severely changed by confining the H atoms between lamellae. Whereas H atom recombination is very efficient on single crystal surfaces, it is very inefficient on the external surfaces of amorphous ice. In micropores, however, the probability of an encounter between two H atoms is greatly increased before the micropore collapse⁶⁶ and even more so after the collapse when the H atoms are confined between two walls in lamellae. In fact, the H atom recombination may be even more efficient than on single crystals because the H atoms have no possibility to desorb from the surface when they are trapped in lamellae.

If the micropores are initially filled with some gases, such as CO, CO_2 , CH_4 or O_2 , which is the case, *e.g.*, for cometary nuclei, the 3D to 2D micropore transition may also provide a natural explanation for the possibility of crystallizing clathrate hydrates *in vacuo* from co-deposits of such gases and ASW.^{67–69} These molecules will have a strong tendency to escape when the micropores collapse, but there is no path to the exterior. The trapping in the lamella will thus result in the buildup of internal pressure, so that the formation of clathrates becomes thermodynamically feasible, in spite of the vacuum environment. These high internal pressures exerted by the lamellae walls on trapped molecules might also affect the chemical processes in interstellar/precometary ices. The high-internal pressure after the collapse to a 2D network of lamellae may hold the key to the riddle how complex organic compounds may form in a relatively short amount of time in interstellar ices in the near-vacuum environment of space and be carried in comets and meteorites as suggested in the “Late Heavy Bombardment” hypothesis for the origins of life.^{70–72} It can also be conceived that the formation of long chain-like molecules, such as interstellar polyynes is strongly favoured when the chemistry takes place in the confined 2D space provided by the lamellae.⁷³ We emphasize, though, that our observations were made on ASW samples deposited at 77 K, whereas the relevant temperatures for formation in astrophysical environments are 10–60 K. The evolution of the pore network and the nature of pore-collapse for samples deposited at lower temperatures will, therefore, be the subject of future studies.

In summary, we have investigated the pore-collapse in differently grown gram-quantities of microporous ASW by

making use of the capabilities of NIMROD, which is the ideal instrument for studying transformations in disordered materials over a broad *Q*-range. The data were analyzed in a model-free approach and by the new Guinier–Porod model. The analysis suggests a sudden transformation from cylindrical (3D) pores to lamellae (2D) at 120 K in the case of baffled ASW samples and 140 K in the case of non-baffled samples. Above 120 K all four samples feature collectively a decrease in the specific surface area, whereas at <120 K pore-clustering is of importance. The radius of gyration of the micropores is found to be about 15 Å, and the periodicity of the pores is on the order of 70 Å. These characteristics of the pore-collapse may be of importance in understanding abiogenesis and understanding of chemical processes in interstellar ices.

Acknowledgements

We gratefully acknowledge the ESF Short visit grant (MicroDICE) for Christian Mitterdorfer and Marion Bauer, and ISIS for access to neutron beam time under the Director's Discretion procedure. We are thankful to Reinhold Pramsoler for designing and constructing additional equipment for the deposition apparatus. TL acknowledges funding by grants from the European Research Council (ERC Starting Grant SULIWA) and the Austrian Science Fund (START award Y391). HJF acknowledges the LASSIE FP7 ITN initiative (Laboratory Astrochemical Surface Science in Europe) grant agreement no. 238258 for her participation in this work.

References

- 1 J. Klinger, *J. Phys. Colloq.*, 1985, **C8**, 657.
- 2 E. Mayer and R. Pletzer, *Nature*, 1986, **319**, 298.
- 3 A. Kouchi, *Nature*, 1987, **330**, 550.
- 4 R. A. Baragiola, *Planet. Space Sci.*, 2003, **51**, 953.
- 5 B. J. Murray and E. J. Jensen, *J. Atmos. Sol.-Terr. Phys.*, 2010, **72**, 51.
- 6 P. Ehrenfreund, H. J. Fraser, J. Blum, J. H. E. Cartwright, J. M. García-Ruiz, E. Hadamcik, A. C. Lvasseur-Regourd, S. Price, F. Prodi and A. Sarkissian, *Planet. Space Sci.*, 2003, **51**, 473.
- 7 S. Ioppolo, H. M. Cuppen, C. Romanzin, E. F. v. Dishoeck and H. Linnartz, *Phys. Chem. Chem. Phys.*, 2010, **12**, 12065.
- 8 H. M. Cuppen, S. Ioppolo, C. Romanzin and H. Linnartz, *Phys. Chem. Chem. Phys.*, 2010, **12**, 12077.
- 9 E. F. Burton and W. F. Oliver, *Nature*, 1935, **135**, 505.
- 10 J. Wenzel, C. U. Linderstrom-Lang and S. A. Rice, *Science*, 1975, **187**, 428.
- 11 J. C. Dore, *J. Mol. Struct.*, 1990, **237**, 221.
- 12 A. Hallbrucker, E. Mayer, L. P. O'Mard, J. C. Dore and P. Chieux, *Phys. Lett. A*, 1991, **159**, 406.
- 13 D. T. Bowron, J. L. Finney, A. Hallbrucker, I. Kohl, T. Loerting, E. Mayer and A. K. Soper, *J. Chem. Phys.*, 2006, **125**, 194502.

- 14 I. Kohl, L. Bachmann, A. Hallbrucker, E. Mayer and T. Loerting, *Phys. Chem. Chem. Phys.*, 2005, **7**, 3210.
- 15 E. Mayer, *J. Appl. Phys.*, 1985, **58**, 663.
- 16 O. Mishima, L. D. Calvert and E. Whalley, *Nature*, 1984, **310**, 393.
- 17 O. Mishima, L. D. Calvert and E. Whalley, *Nature*, 1985, **314**, 76.
- 18 K. Winkel, E. Mayer and T. Loerting, *J. Phys. Chem. B*, 2011, **115**, 14141.
- 19 K. P. Stevenson, G. A. Kimmel, Z. Dohnalek, R. S. Smith and B. D. Kay, *Science*, 1999, **283**, 1505.
- 20 J. H. E. Cartwright, B. Escribano and C. I. Sainz-Diaz, *Astrophys. J.*, 2008, **687**, 1406.
- 21 J.-B. Bossa, K. Isokoski, M. S. d. Valois and H. Linnartz, *Astron. Astrophys.*, 2012, **545**, A82.
- 22 C. G. Venkatesh, S. A. Rice and A. H. Narten, *Science*, 1974, **186**, 927.
- 23 P. Jenniskens and D. F. Blake, *Science*, 1994, **265**, 753.
- 24 W. Hagen, A. G. G. M. Tielens and J. M. Greenberg, *Chem. Phys.*, 1981, **56**, 367.
- 25 V. Buch and J. P. Devlin, *J. Chem. Phys.*, 1991, **94**, 4091.
- 26 B. Rowland, M. Fisher and J. P. Devlin, *J. Chem. Phys.*, 1991, **95**, 1378.
- 27 M. A. Zondlo, T. B. Onasch, M. S. Warshawsky, M. A. Tolbert, G. Mallick, P. Arentz and M. S. Robinson, *J. Phys. Chem. B*, 1997, **101**, 10887.
- 28 L. Schriver-Mazzuoli, A. Schriver and A. Hallou, *J. Mol. Struct.*, 2000, **554**, 289.
- 29 S. La Spisa, M. Waldheim, J. Lintemoot, T. Thomas, J. Naff and M. Robinson, *J. Geophys. Res.: Planets*, 2001, **106**, 33351.
- 30 Ó. Gálvez, B. Maté, V. J. Herrero and R. Escribano, *Icarus*, 2008, **197**, 599.
- 31 R. Pletzer and E. Mayer, *J. Chem. Phys.*, 1989, **90**, 5207.
- 32 P. Ayotte, R. S. Smith, K. P. Stevenson, Z. Dohnalek, G. A. Kimmel and B. D. Kay, *J. Geophys. Res.: Planets*, 2001, **106**, 33387.
- 33 N. Horimoto, H. S. Kato and M. Kawai, *J. Chem. Phys.*, 2002, **116**, 4375.
- 34 C. S. Boxe, B. R. Bodsgard, W. Smythe and M. T. Leu, *J. Colloid Interface Sci.*, 2007, **309**, 412.
- 35 U. Raut, M. Famá, B. D. Teolis and R. A. Baragiola, *J. Chem. Phys.*, 2007, **127**, 204713.
- 36 M. T. Sieger and T. M. Orlando, *Surf. Sci.*, 2000, **451**, 97.
- 37 E. Vichnevetski, A. D. Bass and L. Sanche, *J. Chem. Phys.*, 2000, **113**, 3874.
- 38 M. Tronc and R. Azria, *Int. J. Mass Spectrom.*, 2001, **205**, 325.
- 39 L. Hornekær, A. Baurichter, V. V. Petrunin, A. C. Luntz, B. D. Kay and A. Al-Halabi, *J. Chem. Phys.*, 2005, **122**, 124701.
- 40 L. Amiaud, J. H. Fillion, S. Baouche, F. Dulieu, A. Momeni and J. L. Lemaire, *J. Chem. Phys.*, 2006, **124**, 094702.
- 41 T. Zubkov, R. S. Smith, T. R. Engstrom and B. D. Kay, *J. Chem. Phys.*, 2007, **127**, 184707.
- 42 J.-H. Fillion, L. Amiaud, E. Congiu, F. Dulieu, A. Momeni and J.-L. Lemaire, *Phys. Chem. Chem. Phys.*, 2009, **11**, 4396.
- 43 D. J. Burke and W. A. Brown, *Phys. Chem. Chem. Phys.*, 2010, **12**, 5947.
- 44 M. Eldrup, A. Vehanen, P. J. Schultz and K. G. Lynn, *Phys. Rev. Lett.*, 1983, **51**, 2007.
- 45 Y. C. Wu, A. Kallis, J. Jiang and P. G. Coleman, *Phys. Rev. Lett.*, 2010, **105**, 4.
- 46 Y. C. Wu, J. Jiang, S. J. Wang, A. Kallis and P. G. Coleman, *Phys. Rev. B: Condens. Matter Mater. Phys.*, 2011, **84**, 6.
- 47 A. K. Patra, S. Ramanathan, D. Sen and S. Mazumder, *J. Alloys Compd.*, 2005, **397**, 300.
- 48 E. R. Buiel, A. E. George and J. R. Dahn, *Carbon*, 1999, **37**, 1399.
- 49 G. Walter, R. Kranold, D. Enke and G. Goerigk, *J. Appl. Crystallogr.*, 2003, **36**, 592.
- 50 T. V. Antropova, I. A. Drozdova, T. N. Vasilevskaya, A. V. Volkova, L. E. Ermakova and M. P. Sidorova, *Glass Phys. Chem.*, 2007, **33**, 109.
- 51 D. T. Bowron, A. K. Soper, K. Jones, S. Ansell, S. Birch, J. Norris, L. Perrott, D. Riedel, N. J. Rhodes, S. R. Wakefield, A. Botti, M.-A. Ricci, F. Grazzi and M. Zoppi, *Rev. Sci. Instrum.*, 2010, **81**, 033905.
- 52 J. L. Finney, D. T. Bowron, A. K. Soper, T. Loerting, E. Mayer and A. Hallbrucker, *Phys. Rev. Lett.*, 2002, **89**, 205503.
- 53 J. L. Finney, A. Hallbrucker, I. Kohl, A. K. Soper and D. T. Bowron, *Phys. Rev. Lett.*, 2002, **88**, 225503.
- 54 K. Winkel, D. T. Bowron, T. Loerting, E. Mayer and J. L. Finney, *J. Chem. Phys.*, 2009, **130**, 204502.
- 55 E. Mayer and R. Pletzer, *J. Chem. Phys.*, 1984, **80**, 2939.
- 56 M. P. Collings, J. W. Dever, H. J. Fraser, M. R. S. McCoustra and D. A. Williams, *Astrophys. J.*, 2003, **583**, 1058.
- 57 E. Mayer, *J. Mol. Struct.*, 1991, **250**, 403.
- 58 G. P. Johari, A. Hallbrucker and E. Mayer, *J. Chem. Phys.*, 1991, **95**, 2955.
- 59 E. Mayer, *J. Phys. Chem.*, 1985, **89**, 3474.
- 60 E. Mayer and R. Pletzer, *J. Chem. Phys.*, 1985, **83**, 6536.
- 61 O. L. Spalla and F. Testard, *J. Appl. Crystallogr.*, 2003, 338.
- 62 B. Hammouda, *J. Appl. Crystallogr.*, 2010, **43**, 716.
- 63 G. Paglia, C. E. Buckley, T. J. Udovic, A. L. Rohl, F. Jones, C. F. Maitland and J. Connolly, *Chem. Mater.*, 2004, **16**, 1914.
- 64 D. D. Hass, H. Zhao, T. Dobbins, A. J. Allen, A. J. Slifka and H. N. G. Wadley, *Mater. Sci. Eng., A*, 2010, **527**, 6270.
- 65 B. Hammouda, *Eur. Polym. J.*, 2010, **46**, 2275.
- 66 E. Mayer and R. Pletzer, *J. Phys. Colloq.*, 1987, **48**, 581.
- 67 A. Hallbrucker and E. Mayer, *J. Chem. Soc., Faraday Trans.*, 1990, **86**, 3785.
- 68 A. Hallbrucker and E. Mayer, *Icarus*, 1991, **90**, 176.
- 69 D. Blake, L. Allamandola, S. Sandford, D. Hudgins and F. Freund, *Science*, 1991, **254**, 548.
- 70 M. P. Bernstein, J. P. Dworkin, S. A. Sandford and L. J. Allamandola, *Meteorit. Planet. Sci.*, 2001, **36**, 351.
- 71 J. P. Dworkin, D. W. Deamer, S. A. Sandford and L. J. Allamandola, *Proc. Natl. Acad. Sci. U. S. A.*, 2001, **98**, 815.
- 72 S. Kwok and Y. Zhang, *Nature*, 2011, **479**, 80.
- 73 W. W. Duley and D. A. Williams, *Mon. Not. R. Astron. Soc.*, 1984, **211**, 97.